Case C2.2: Turbulent, Transonic Flow over an RAE 2822 Airfoil

Masayuki Yano* and David L. Darmofal†

Aerospace Computational Design Laboratory, Massachusetts Institute of Technology

I. Code Description

ProjectX is a high-order, adaptive discontinuous Galerkin finite element solver. The DG discretization uses Roe's approximate Riemann solver[1] for the inviscid numerical flux, Bassi and Rebay's second discretization (BR2)[2] for the viscous numerical flux, and Oliver's asymptotically dual-consistent discretization[3] for the RANS source term. Modifications have been made to the Spalart-Allmaras turbulence model[4] as described by Oliver[5] to improve robustness of the RANS model for higher-order discretizations. (The model incorporates few additional modifications by Modisette.[6]) To regularize the shocks, artificial viscosity is added in a smooth manner using a jump-based discontinuity sensor and the shock PDE introduced by Barter and Darmofal[7] with a few additional modifications.[8]

The solution to the discretized system is obtained using a Newton-based nonlinear solver with pseudo-time continuation and a line search on unsteady residual that explicitly controls the accuracy of time integration.[6,8] The combination improves solver robustness, particularly through initial transients and on coarse meshes. The linear system arising in each pseudo-time step is solved using GMRES,[9] preconditioned with an in-place block-ILU(0) factorization[10] with minimum discarded fill reordering and $p = 0$ algebraic coarse correction.[11]

An output-based, anisotropic simplex adaptation algorithm is used to control the discretization error.[12] The algorithm iterates toward a mesh that minimizes the output error for a given number of degrees of freedom. The anisotropic adaptation decisions are entirely driven by the behavior of an output-based *a posteriori* error estimate; thus, the method handles any discretization order, naturally incorporates both the primal and adjoint solution behaviors, and robustly treats irregular features. The output error estimate uses the dual-weighted residual (DWR) method of Becker and Rannacher.[13] A new mesh that conforms to the metric request is generated using using BAMG (Bidimensional Anisotropic Mesh Generator),[14] and higher-order, globally curved meshes are constructed through linear elasticity.[3]

II. Case Description

II.A. Flow Condition

This case considers transonic, turbulent flow over an RAE 2822 airfoil, with a freestream Mach number of $M_\infty = 0.734$, angle of attack of $\alpha = 2.79^\circ$, and Reynolds number based on chord of $Re_c = 6.5 \times 10^6$. The dynamic viscosity is assumed to adhere to Sutherland's law, the Prandtl number is set to $Pr = 0.71$, and the freestream turbulence level is set to $\rho_\infty \tilde{\nu}_\infty = 5.0 \rho_\infty \nu_\infty$.

II.B. Domain Specification

A square outer domain with the half-edge length of $R = 10000c$ is used for this case (i.e. the square is $20000c \times 20000c$). To minimize the effect of the farfield boundary location, the flux at farfield boundaries is determined using the Roe flux in which the exterior state is set to the freestream conditions (instead of specifying the stagnation quantities and flow angle at the inflow and the static pressure at the outflow).[15]

*Doctoral candidate, 77 Massachusetts Ave. 37-442, Cambridge, MA, 02139, myano@mit.edu

†Professor, 77 Massachusetts Ave. 37-451, Cambridge, MA, 02139, darmofal@mit.edu

II.C. Convergence Criterion

The ℓ^2 norm of the DG residual of non-dimensionalized Navier-Stokes equations is used to monitor convergence to the steady state. Our solver operates on non-dimensionalized variables

$$\rho^* = \frac{\rho}{\rho_\infty}, \quad u^* = \frac{u}{\|V_\infty\|}, \quad v^* = \frac{u}{\|V_\infty\|}, \quad p^* = \frac{p}{\rho_\infty \|V_\infty\|^2}, \quad e^* = \frac{e}{\|V_\infty\|^2},$$
$$R^* = \frac{R}{c_v}, \quad T^* = \frac{T}{\|V_\infty\|^2/c_v}, \quad \text{and} \quad \mu^* = \frac{\mu}{\rho_\infty L_\infty V_\infty}.$$

The DG residual is computed against the Lagrange test functions with equidistributed nodes, and the ℓ^2 norm of the residual is converged to 1×10^{-9}. (Note that the solver time would not be significantly influenced for any reasonable choice of the tolerance (say $< 1 \times 10^{-7}$), as we achieve Newton convergence in this regime. With the specified non-dimensionalization, the difference between the ℓ^2 residual and the mass residual is well within this offset.)

II.D. Hardware Specification

All computations are performed in serial on a Linux machine with an Intel i7-2600 processor and 16 Gbytes of RAM. The machine produces a Taubench time of 6.60 seconds.

II.E. Residual Timing

The time for performing a single dof $= 250,000$ residual evaluation, including the full Jacobian construction for the implicit solver, is summarized in Table 1. The residual evaluation is performed on a 14285-element mesh and the times are scaled to 250,000 degrees of freedom.

p	time (work unit)
1	8.15
2	6.14
3	6.15

Table 1. dof $= 250,000$ residual evaluation time (including the full Jacobian construction).

II.F. Initial Mesh

The initial mesh used for this case is shown in Figure 1. The airfoil geometry is represented using $q = 3$ simplex elements. Note that the mesh does not have any refinement in the boundary layer region and is unsuited for RANS calculation. Our objective is to demonstrate a fully-automated transition to a RANS mesh using the adaptive algorithm. After each mesh refinement, the geometry representation is refined by re-sampling from a fine cubic spline defining the RAE 2822 geometry.

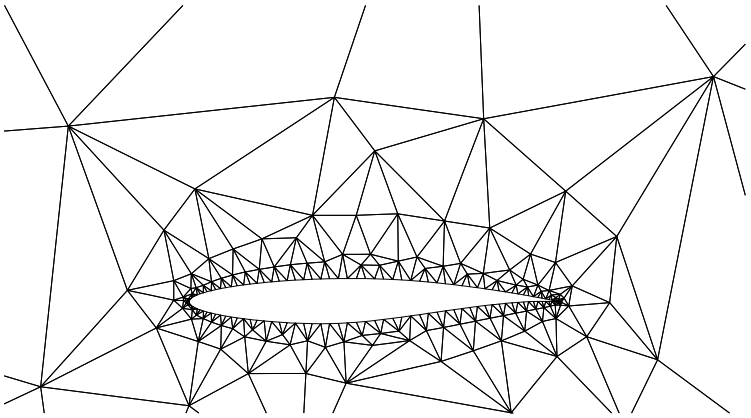

Figure 1. The initial 520-element mesh.

II.G. Adaptation Procedure and Data Reported

For each solution order p, the numbers of degrees of freedom considered are:

$$p = 1, 2, \quad \text{dof} = \{20000, 40000, 80000, 120000\}$$
$$p = 3, \quad \text{dof} = \{40000, 80000, 120000\}.$$

For each p-dof combination, a family of optimized meshes are generated using our anisotropic simplex mesh adaptation algorithm.[12] The output adapted is the drag on the airfoil.

Unlike the simple flows considered in C1.X, it is difficult to converge the nonlinear problem resulting from the $p > 1$ discretizations on coarse meshes with no boundary layer resolution. In particular, in fully-automated adaptation, the solver must find a solution on every mesh encountered in the adaptive sequence without a single failure. Our $p > 1$ RANS solver currently does not have this level of robustness. To overcome the lack of robustness, we make the initial transition from the coarse isotropic mesh, shown in Figure 1, to a coarse RANS mesh, with some boundary layer resolution, using the $p = 1$ discretization. Then, the $p = 2$ and $p = 3$ adaptation are initialized from the coarse $p = 1$ RANS mesh.

The drag error variation during this initial transition process for the $p = 2$, dof $= 20,000$ combination is shown in Figure 2. Starting from the initial mesh shown in Figure 1, seven $p = 1$, dof $= 10,000$ adaptation iterations are performed to produce a $p = 1$ mesh shown in Figure 3(a). The mesh is still very coarse, as reflected in the drag error of 10 counts, but the boundary layer is sufficiently refined such that the $p = 2$ adaptation sequence can be initialized and carried out in a reliable manner. After 11 additional $p = 2$, dof $= 20,000$ adaptation iterations, we obtain a $p = 2$, dof $= 20,000$ optimized mesh, shown in Figure 3(b), that achieves less than 0.2 counts of drag error. This mesh is used as the starting mesh for the all higher-dof $p = 2$ cases.

Similarly, the $p = 3$ adaptation sequence is started from the coarse $p = 1$ RANS mesh shown in Figure 3(a). The starting dof used for the $p = 3$ adaptation is dof $= 40,000$.

As in Case 1.1, the performance of each p-dof is assessed by averaging the error obtained on five realization of meshes in the family. The time reported is the total time required to reach the first realization of the p-dof-optimized mesh starting from the initial mesh shown in Figure 1; this includes multiple flow solves and adaptation overhead. For example, the time to perform the entire 18 adaptation cycles is reported for the $p = 2$, dof $= 20,000$ case, whose drag error history is shown in Figure 2. (See the description provided in Case 1.1 for details on the error assessment procedure.)

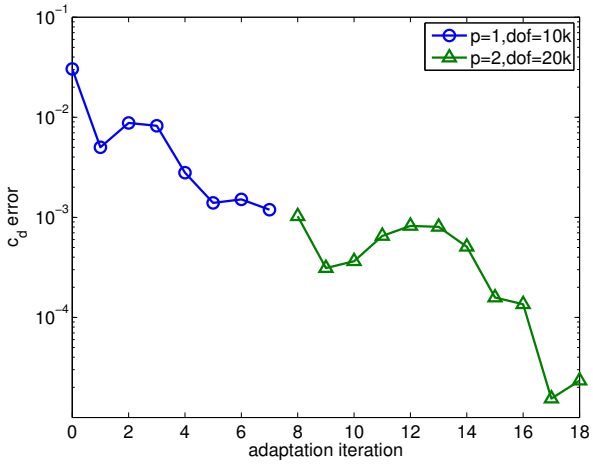

Figure 2. The drag coefficient history starting from the initial mesh shown in Figure 1.

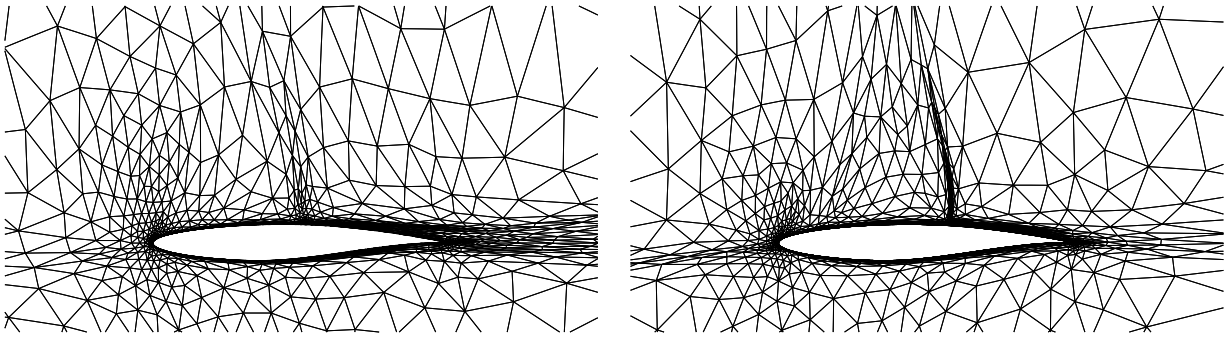

(a) $p = 1$, dof $= 10,000$, $\mathcal{E}_{c_d} = 1.0 \times 10^{-3}$ (b) $p = 2$, dof $= 20,000$, $\mathcal{E}_{c_d} = 1.8 \times 10^{-5}$

Figure 3. Meshes obtained after the initial transition.

III. Results

III.A. Error Convergence

The reference solution is obtained using the adaptive $p = 4$, dof $= 320,000$ discretization. The reference c_d and c_l values used for this case are

$$c_d = 0.01842695 \pm 2 \times 10^{-8}$$
$$c_l = 0.823093.$$

The error estimate for c_d is based on the adjoint-based error estimate and the fluctuation in the c_d value for this family of optimized meshes.

Figure 4(a) shows the convergence of the drag coefficient against the number of degrees of freedom. The $p > 1$ discretizations are more efficient that the $p = 1$ discretizations for simulations requiring less than 0.5 drag counts of error. In particular, the $p > 1$ discretization significantly reduces the number of degrees of freedom required to achieve higher fidelity. This is in contrast to the transonic inviscid flow over a NACA 0012 considered in Case 1.3, in which higher-order discretizations is ineffective. In the transonic RANS problem, the drag is dictated not only by the transonic shock but also by the boundary layer. As the higher-order discretizations are effective at resolving the boundary layer, even though the shock resolution itself it not improved, the $p > 1$ discretizations are overall more efficient than the $p = 1$ discretization. However, the $p = 3$ discretization is not any more efficient than the $p = 2$ discretization even at the error level of as low as 0.001 drag counts.

Figure 4(b) shows that, for high-fidelity simulations, the higher-order discretizations are more efficient than the $p = 1$ discretization also in terms of the work unit. As indicated by the absence of the data points in the first 1000 work unit, a relatively large fraction of the time is spent on performing the initial Euler-to-RANS mesh transition. Figures 4(c) and 4(d) show that the $p > 1$ discretizations are more efficient than the $p = 1$ discretization in also predicting the lift.

III.B. Adapted Meshes

Examples of drag-adapted meshes are shown in Figure 5. Various features in the primal and adjoint solutions are resolved through adaptive refinement, including: the boundary layers, stagnation streamline, wake, shock, trailing edge singularity, and the SA irregularity at the outer edge of the boundary layers. The refinements toward these features are clearly seen in Figure 6.

Comparison of the $p = 1$, dof $= 80,000$ mesh (Figure 5(a)) and the $p = 2$, dof $= 20,000$ mesh (Figure 5(b)) reveals the diffeences in the meshes required to achieve the drag error level of approximately 3×10^{-5} using the $p = 1$ and $p = 2$ discretizations. Compared to the $p = 1$ mesh, the $p = 2$ mesh is sparse in the region outside of the shock and the boundary layers.

Comparison of the $p = 2$, dof $= 20,000$ mesh (Figure 5(b)) and the $p = 2$, dof $= 80,000$ (Figure 5(c)) mesh shows how the mesh evolves for a given p to achieve a lower error level. In addition to the boundary layers and the shock, the adaptation algorithm targets the wake, the stagnation streamline, and the Λ-like feature inside the sonic pocket in the adjoint. Comparing the close up of the $p = 2$, dof $= 80,000$ mesh

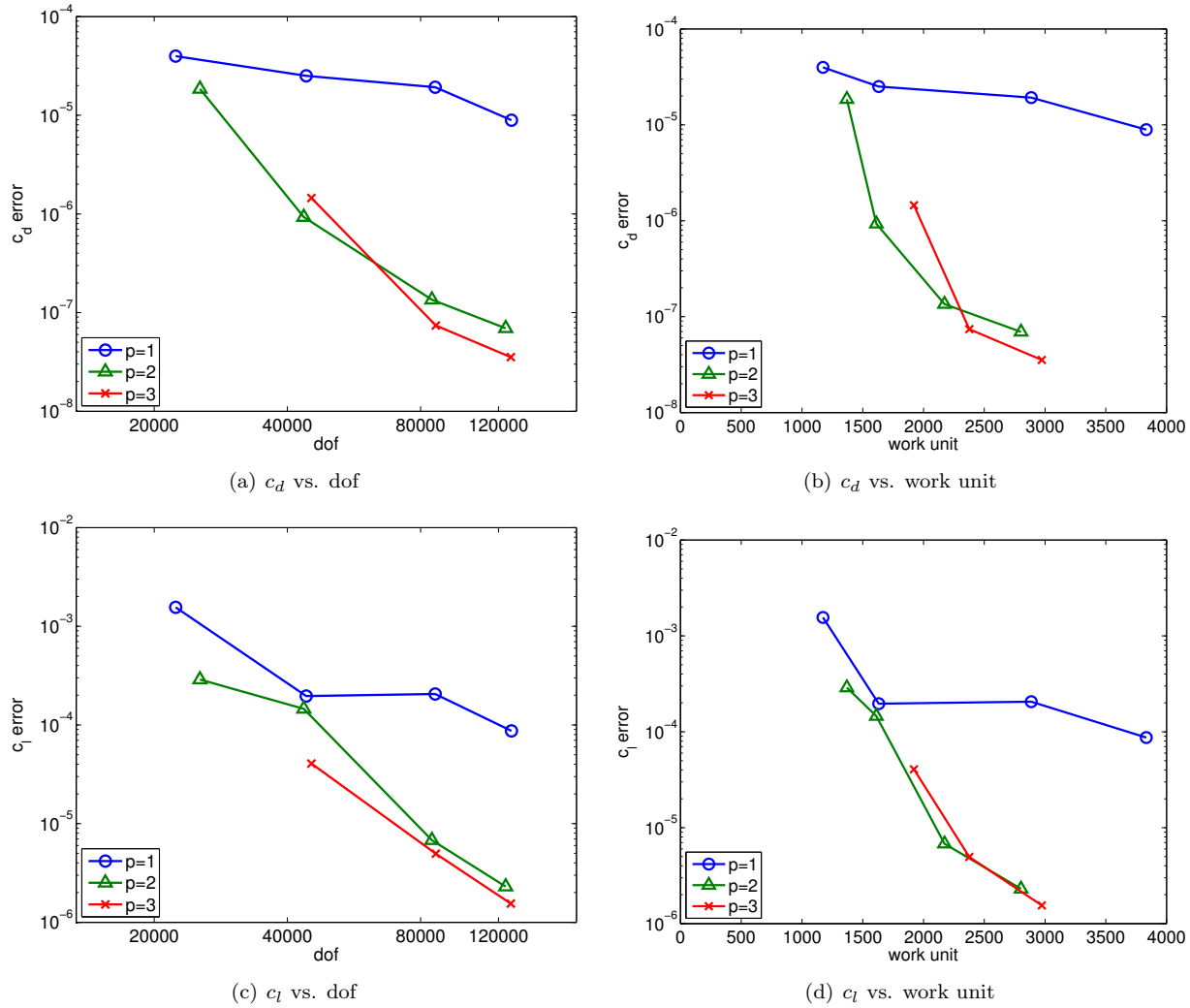

(a) c_d vs. dof

(b) c_d vs. work unit

(c) c_l vs. dof

(d) c_l vs. work unit

Figure 4. Error convergence.

shown in Figure 6 and the solutions shown in Figure 7, adaptive refinement of both the primal and adjoint features is evident.

III.C. Uniform vs. Adaptive Refinement

Figure 8 compares the drag error convergence results obtained using adaptive refinement and a step of uniform refinement starting from a select adapted meshes. For the $p = 1$ discretization, adaptive refinement does not make a significant difference when the mesh is already optimized at a lower number of degrees of freedom. Note that this does not mean that adaptive refinement does not make a difference; the starting mesh for the step of uniform refinement is still a highly adapted mesh optimized for this case. On the other hand, for $p = 2$, a step of uniform refinement is insufficient to realize the full potential of the higher-order discretization, even if the mesh is optimized at a lower degrees of freedom. All subsequent refinement must be performed adaptively to control the effect of multiple singularities in the solution.

Figure 9 shows the timing breakdown of the adaptation overhead relative to the primal solve (i.e the flow solve). The adaptation overhead is a smaller fraction of the entire solution process for this medium-sized problem, compared to that observed in small problems (c.f. C1.1 and C1.2). Considering the accuracy-per-dof benefit of adaptation, the additional cost is justified.

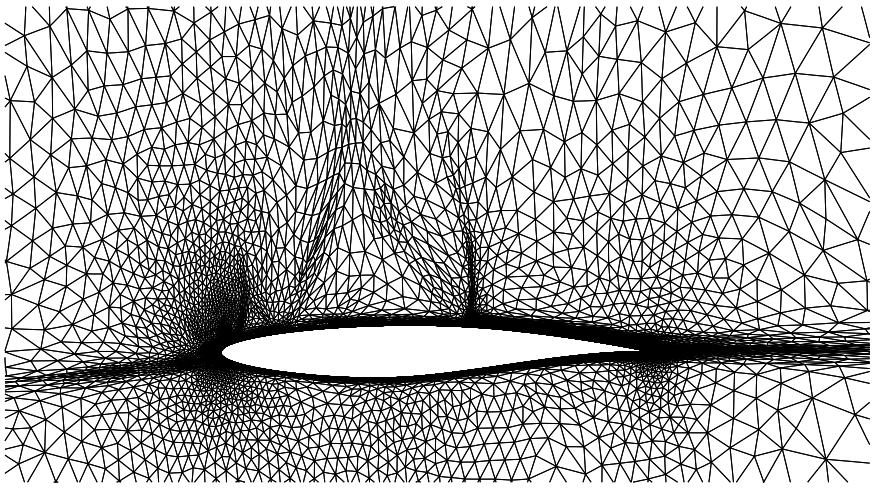

(a) $p = 1$, dof $= 80,000$, $\mathcal{E}_{c_d} = 1.9 \times 10^{-5}$

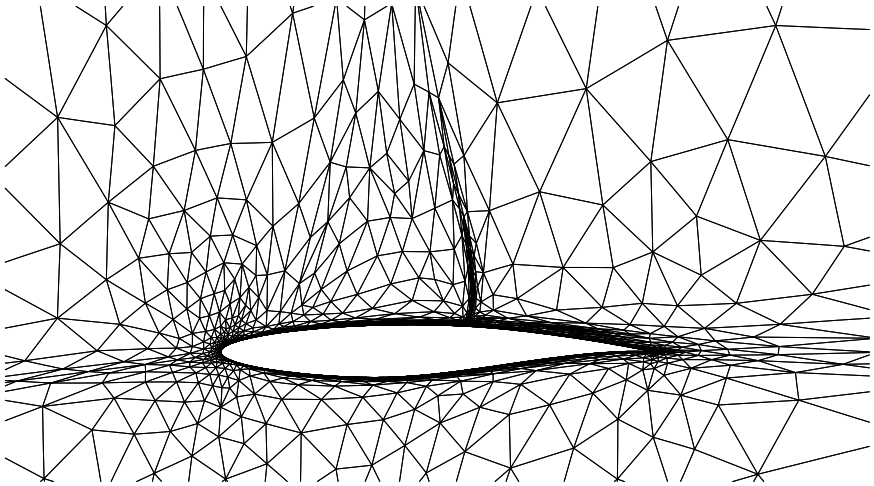

(b) $p = 2$, dof $= 20,000$, $\mathcal{E}_{c_d} = 1.8 \times 10^{-5}$

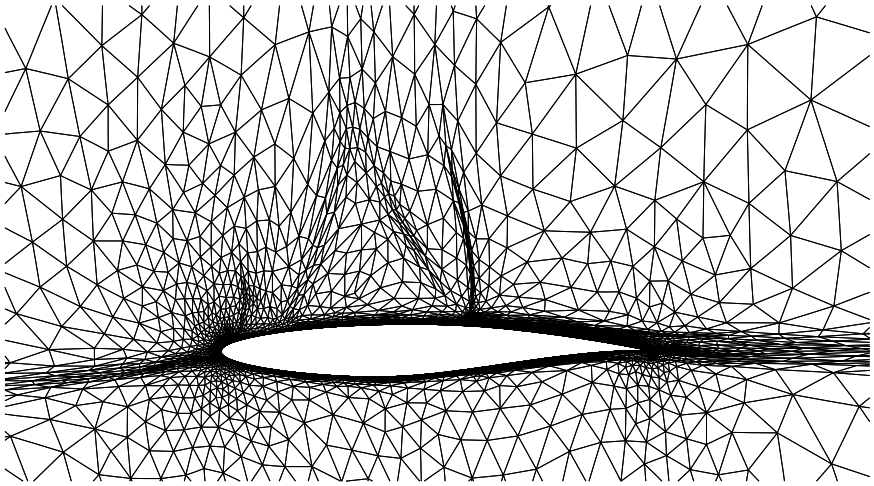

(c) $p = 2$, dof $= 80,000$, $\mathcal{E}_{c_d} = 1.4 \times 10^{-7}$

Figure 5. Select adapted meshes.

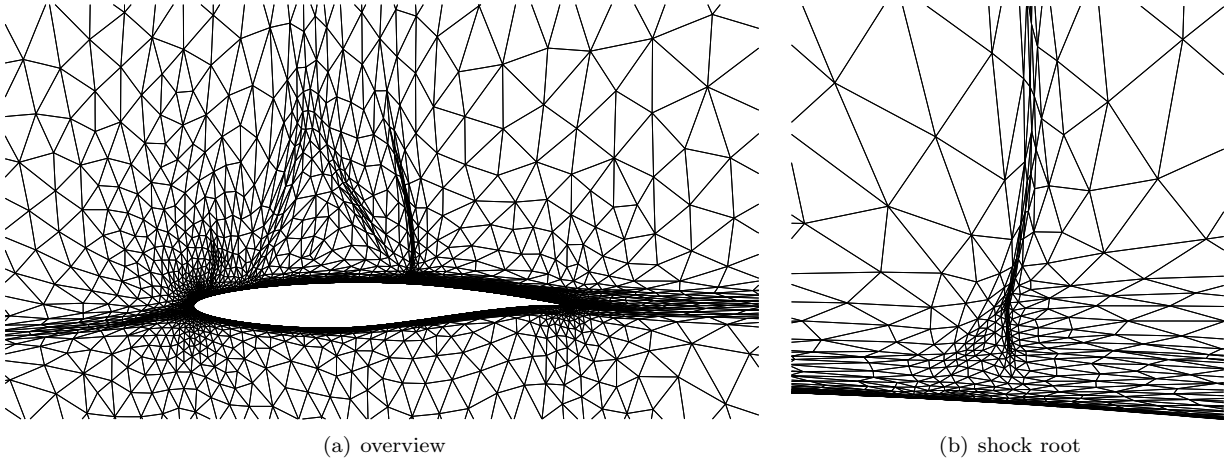

(a) overview (b) shock root

(c) leading edge (d) trailing edge

Figure 6. Close up of different regions of the $p = 2$, dof $= 80,000$ drag-adapted mesh.

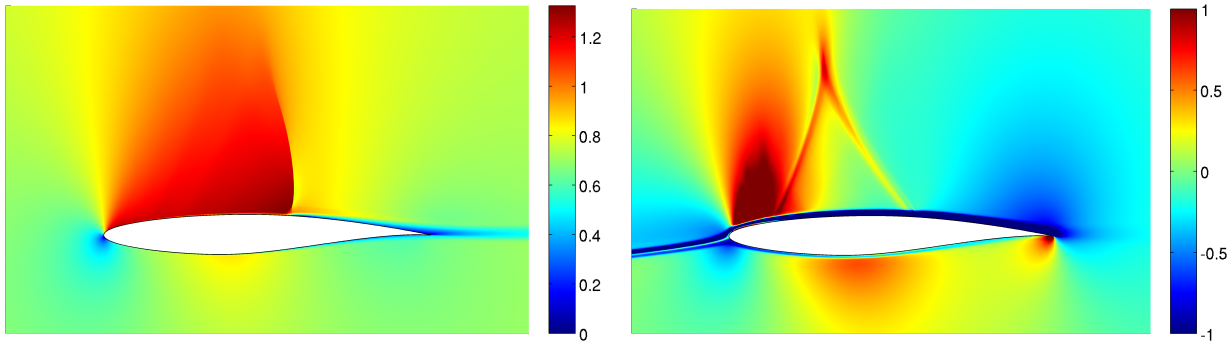

(a) Mach number (b) mass adjoint (drag output)

Figure 7. The Mach number distribution and the mass adjoint for the drag output.

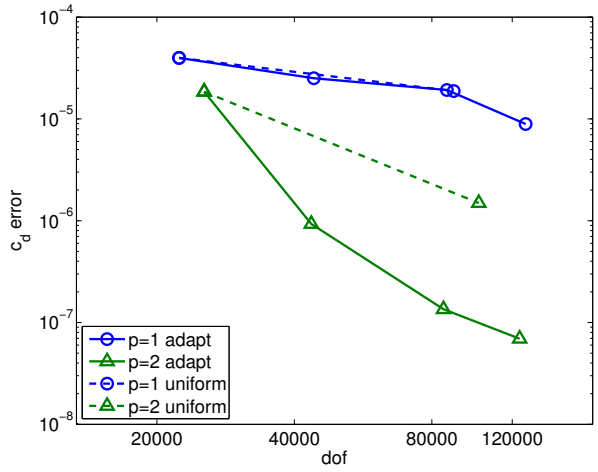

Figure 8. Comparison of adaptive refinement and a step of uniform refinement starting from an adapted mesh.

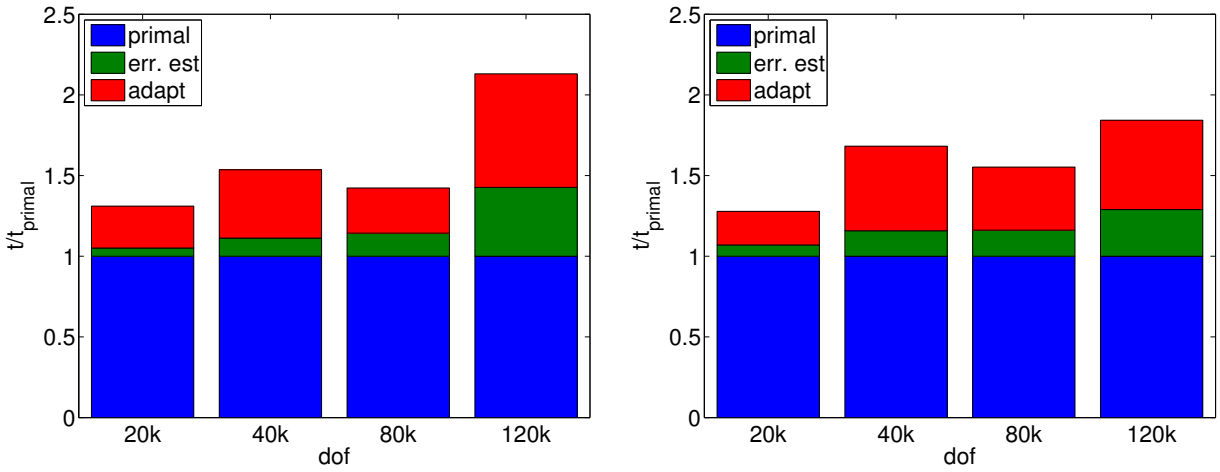

(a) $p = 1$ (b) $p = 2$

Figure 9. Timing breakdown.

III.D. Surface Quantity Distributions

The pressure and skin friction coefficient distributions are shown in Figure 10. Both distributions are smooth, and the rapid change in the coefficients across the shock are captured well. Note that there is a small region of recirculation after the shock.

Acknowledgments

The authors would like to thank the entire ProjectX team for the many contributions that enabled this work. Special thanks goes to Dr. Steven Allmaras for insightful discussions that led to improved robustness of the RANS-SA solver. This work was supported by the Singapore-MIT Alliance Fellowship in Computational Engineering and The Boeing Company with technical monitor Dr. Mori Mani.

References

[1]P. L. Roe, Approximate Riemann solvers, parameter vectors, and difference schemes, J. Comput. Phys. 43 (2) (1981) 357–372.

[2]F. Bassi, S. Rebay, GMRES discontinuous Galerkin solution of the compressible Navier-Stokes equations, in: K. Cockburn,

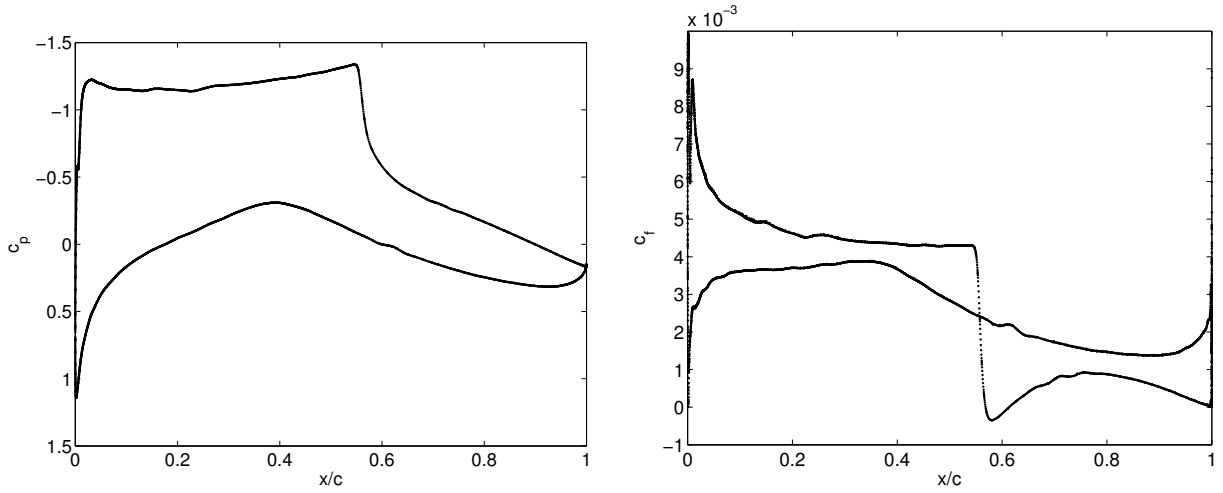

(a) pressure coefficient

(b) skin friction coefficient

Figure 10. The pressure and skin friction coefficient distributions.

Shu (Eds.), Discontinuous Galerkin Methods: Theory, Computation and Applications, Springer, Berlin, 2000, pp. 197–208.

[3]T. A. Oliver, A higher-order, adaptive, discontinuous Galerkin finite element method for the Reynolds-averaged Navier-Stokes equations, PhD thesis, Massachusetts Institute of Technology, Department of Aeronautics and Astronautics (Jun. 2008).

[4]P. R. Spalart, S. R. Allmaras, A one-equation turbulence model for aerodynamics flows, AIAA 1992-0439 (Jan. 1992).

[5]T. Oliver, D. Darmofal, Impact of turbulence model irregularity on high-order discretizations, AIAA 2009-953 (2009).

[6]J. M. Modisette, An automated reliable method for two-dimensional Reynolds-averaged Navier-Stokes simulations, PhD thesis, Massachusetts Institute of Technology, Department of Aeronautics and Astronautics (2011).

[7]G. E. Barter, D. L. Darmofal, Shock capturing with pde-based artificial viscosity for dgfem: Part i, formulation, J. Comput. Phys. 229 (5) (2010) 1810–1827.

[8]M. Yano, J. M. Modisette, D. Darmofal, The importance of mesh adaptation for higher-order discretizations of aerodynamic flows, AIAA 2011–3852 (Jun. 2011).

[9]Y. Saad, M. H. Schultz, GMRES: A generalized minimal residual algorithm for solving nonsymmetric linear systems, SIAM Journal on Scientific and Statistical Computing 7 (3) (1986) 856–869.

[10]L. T. Diosady, D. L. Darmofal, Preconditioning methods for discontinuous Galerkin solutions of the Navier-Stokes equations, J. Comput. Phys. 228 (2009) 3917–3935.

[11]P.-O. Persson, J. Peraire, Newton-GMRES preconditioning for discontinuous Galerkin discretizations of the Navier-Stokes equations, SIAM J. Sci. Comput. 30 (6) (2008) 2709–2722.

[12]M. Yano, D. Darmofal, An optimization framework for anisotropic simplex mesh adaptation: application to aerodynamic flows, AIAA 2012–0079 (Jan. 2012).

[13]R. Becker, R. Rannacher, An optimal control approach to a posteriori error estimation in finite element methods, in: A. Iserles (Ed.), Acta Numerica, Cambridge University Press, 2001.

[14]F. Hecht, Bamg: Bidimensional anisotropic mesh generator,
`http://www-rocq1.inria.fr/gamma/cdrom/www/bamg/eng.htm` (1998).

[15]S. R. Allmaras, V. Venkatakrishnan, F. T. Johnson, Farfield boundary conditions for 2-d airfoils, AIAA 2005-4711 (2005).